





Composition- And Size- Controlled I-V-VI Semiconductor Nanocrystals

Journal Article

Author(s):

Yarema, Olesya ; Yarema, Maksym ; Moser, Annina ; Enger, Olivier; Wood, Vanessa 

Publication date:

2020-03-10

Permanent link:

<https://doi.org/10.3929/ethz-b-000406659>

Rights / license:

[In Copyright - Non-Commercial Use Permitted](#)

Originally published in:

Chemistry of Materials 32(5), <https://doi.org/10.1021/acs.chemmater.9b05191>

Funding acknowledgement:

175889 - Multi-length Scale Engineering of Thermal Properties of Nanocrystals and their Composite Films: Fundamentals and Applications (SNF)

161249 - Colloidal nanocrystals of intermetallic compounds and alloys for phase-change memory applications (SNF)

Composition and Size Controlled I-V-VI Semiconductor Nanocrystals

Olesya Yarema,[†] Maksym Yarema,[†] Annina Moser,[†] Olivier Enger,[‡] and Vanessa Wood^{†,*}

[†] Materials and Device Engineering Group, Department of Information Technology and Electrical Engineering, ETH Zurich, CH-8092 Zurich, Switzerland

[‡] BASF Switzerland AG, Klybeckstrasse 141, CH-4057 Basel, Switzerland

ABSTRACT: Non-isovalent ternary and quaternary semiconductors (i.e., having two or more cations with different valence) have unique structural and electronic properties that are leveraged in photovoltaic, thermoelectric, and phase-change memory devices. Making these complex semiconductors in the form of colloidal nanocrystals imparts size-dependent properties and solution processability. Here, we present results on I-V-VI group colloidal nanocrystals. We focus on achieving sub-10 nm sizes for a wide range of I-V-VI selenide nanocrystals, including AgSbSe₂, AgSb₂Se₃, CuSbSe₂, Cu₃SbSe₄, AgBiSe₂, and CuBiSe₂. To highlight one possible application for these I-V-VI colloidal nanomaterials, we analyze the optical absorption and show that through composition and size control, this class of materials offers bandgaps in the mid- to near-IR. Absorption coefficients of AgSbSe₂, CuSbSe₂, and Cu₃SbSe₄ nanocrystals are on par with or higher than the well-studied PbS nanocrystals highlighting their potential for devices such as solar cells, (mid-)infrared photodetectors, and near-infrared bio-imaging systems.

INTRODUCTION

Non-isovalent I-V-VI group ternary semiconductors are promising candidates for optoelectronic, thermoelectric, and phase-change memory applications.¹⁻⁷ I-V-VI materials have narrow band gaps and very high absorption coefficients (e.g., compared to commonly used CuInSe₂ photovoltaic material, the I-V-VI analogue, CuSbSe₂, has a similar band gap but is more absorptive in the whole spectral region).^{2,3} I-V-VI materials also exhibit high thermoelectric figures of merit (ZT).⁴⁻⁶ In AgSbSe₂ and AgSbTe₂, for example, this is due to their good electrical conductivity but low thermal conductivity stemming from bond anharmonicity and strong phonon-phonon interactions.⁸ ZT can be optimized by tuning the composition, e.g., via alloying with binary GeTe and PbTe or by doping with Bi or Cd⁹⁻¹¹ thereby adjusting the carrier concentrations. Finally, I-V-VI materials are interesting for phase-change memory applications because they can exist in amorphous and crystalline phases (e.g., AgSbSe₂ has one of the largest resistivity contrasts with more than 4 orders of magnitude between the amorphous and crystalline phases).⁷

When multicomponent semiconductors are realized in form of nanocrystals, one can engineer properties through both composition and size.^{12,13} For example, in the case of I-III-VI colloidal nanocrystals, for which we developed a synthesis with independent control over the size and the composition,^{14,15} we showed that the optical properties of I-III-VI nanocrystals (e.g., optical band gap, emission peak wavelength, and luminescence efficiency) can be tuned not only by size but also by composition (i.e., tuning the ratio between Group I and Group III elements in the I-III-VI

structure).¹² Particularly, we observed enhanced luminescence efficiencies at some I-III-VI stoichiometries, for which ordering of cationic sublattice can be realized.^{12,14,15} This example highlights the importance of investigating the composition-dependent properties of multicomponent nanomaterials and developing syntheses that enable independent size and composition tuning across the ternary phase-diagram.

Colloidal I-V-VI nanocrystals have already been shown to offer potentially rich functionality.¹⁶⁻²¹ For example, AgBiS₂ nanocrystals have been used to prepare solar cells with efficiency of 6.3%.¹⁶ As in the bulk, AgBiS₂ nanocrystals are highly absorptive, such that only a 37 nm nanocrystal absorber layer is necessary. Furthermore, colloidal AgSbSe₂ and Cu₃SbSe₄ nanocrystals have been used in thermoelectric devices.^{17,18} The efficiency of nanocrystal-based I-V-VI thermoelectrics has been improved through the doping with Bi and Sn, reaching ZT > 1 at medium temperature range of 600-700°C for AgSb_{0.98}Bi_{0.02}Se₂ and Cu₃Sb_{0.88}Sn_{0.10}Bi_{0.02}Se₄ compositions.^{17,18}

Despite these successful application cases,¹⁶⁻¹⁸ colloidal I-V-VI nanocrystals remain relatively little developed. In particular, there are only a handful of research articles reporting I-V-VI selenide nanocrystals, while some selenide compositions, such as Cu-Bi-Se, and all I-V-VI tellurides are not reported in form of colloidal nanoparticles.^{17,18,21-23} Furthermore, most of existing recipes result in large I-V-VI sizes.¹⁷ Finally, focus has been placed on the stoichiometric ternary phases, such as AgSbSe₂ or Cu₃SbSe₄,^{17,18,22} which leaves out the large compositional variety enabled by tuning the ratio between the Group I and Group V cations.

The main synthetic challenge for non-isovalent nanocrystals is to balance the reactivity of different molecular metal precursors in the reaction mixture.¹² Having different valence, these metal sources often possess distinctly different coordination numbers, chemical affinities to coordinating ligands and chalcogen precursors, steric effects, etc. Reactivity balance can be achieved, for example, by judicious choice of metal salts with similar reactivity, by adjusting their reactivity with a choice and a concentration of complexants, or by using highly reactive reagents or mediums (i.e., reducing agents, promoting agents, etc.).¹²

The synthesis of Ag-Sb-Se nanocrystals illustrates this challenge. To date, only two papers report colloidal AgSbSe₂ nanocrystals with narrow size distributions.^{17, 22} The synthesis of Cabot and co-workers¹⁷ relies on use of oleylamine and oleic acid mixture to passivate Ag and Sb salts, respectively. The use of strongly-bound oleic acid surfactant; however, makes it necessary to use high reaction temperature, leading to nanocrystals in the 7-17 nm size range.¹⁷ Snee and co-workers²² increased the reactivity of Sb (III), using organometallic precursor with easy-leaving silylamide groups. This reaction scheme also leads to large AgSbSe₂ nanocrystals, about 9 nm in diameter.²²

Here, we demonstrate a synthetic approach for engineering the composition and size of sub-10 nm I-V-VI nanocrystals. We first focus on Ag-Sb-Se nanocrystals, and achieve composition control for nanocrystals, those size can be controlled between 2 and 7 nm in diameter. Accurate composition series for Ag-Sb-Se nanocrystals allow for the detection of the broad solid solution, exhibiting rock salt crystal structure. Although such solid solution is reported for bulk Ag-Sb-Se,²⁴ for nanocrystals it spans notably larger composition range and lays on 50 at.% iso-concentration line of Se (i.e., belongs to Ag_xSb_{1-x}Se solid solution). We then expand the synthetic strategy to other I-V-VI nanocrystals, including CuSbSe₂, Cu₃SbSe₄, AgBiSe₂, and CuBiSe₂. Finally, we assess the optical absorption of these materials to highlight their potential application in infrared photodetectors.

EXPERIMENTAL SECTION

Materials. Antimony (III) chloride (99.999 %, STREM), Bismuth (III) chloride (99.999 %, STREM), Copper (I) chloride (99.99 %, Sigma-Aldrich), Silver iodide (99.999 %, Alfa Aesar), 1-dodecanethiol (98 %, Sigma-Aldrich), oleylamine (techn. 80-90 %, Acros), selenium (shots, 99.99 %, STREM), chloroform (anhydrous, >99 %, Sigma-Aldrich), and ethanol (anhydrous, 99.9%, Acros). Oleylamine was dried under vacuum at 100°C for 1 h. Selenium stock solution was prepared by dissolving 0.395 g of Se powder (5 mmol) in 10 mL of a 1:1 mixture of dodecanthiol and oleylamine. All chemicals were stored in inert atmosphere.

Synthesis of Ag-Sb-Se nanocrystals. In a typical synthesis of Ag-Sb-Se nanocrystals, 0.117 g of AgI (0.5 mmol) and 0.114 g of SbCl₃ (0.5 mmol) were dissolved in 7 mL of dried oleylamine in a nitrogen-filled glovebox. This solution of metal salt precursors was then transferred to the three-

neck flask and additionally purified at 90°C and under vacuum during 30 min. Next, the reaction flask was backfilled with nitrogen and the reaction temperature was set between 30 and 150°C. After temperature equilibration, 2 mL of 0.5M Se stock solution (in 1:1 oleylamine:dodecanethiol mixture) was injected at the chosen set temperature. Reaction between 3 and 30 min were allowed and were terminated by rapid cooling or dilution with anhydrous chloroform.

Composition control for Ag-Sb-Se nanocrystals was achieved by adjusting the ratio of AgI and SbCl₃ in the reaction flask. The total concentration of metal salts was kept constant at 1 mmol. The amount of Se precursor was equimolar for all syntheses, i.e., $n[\text{Se}] = 0.5 \cdot n(\text{AgI}) + 1.5 \cdot n(\text{SbCl}_3)$. For example, to synthesize AgSb₂Se₃ nanocrystals, the following total amounts of elemental precursors were introduced: $n(\text{AgI}) = 0.3$ mmol, $n(\text{SbCl}_3) = 0.7$ mmol, $n(\text{Se}) = 1.2$ mmol.

As-prepared Ag-Sb-Se nanocrystals were transferred to air-free gloveboxes and purified under inert atmosphere using anhydrous chloroform and anhydrous ethanol, followed by the centrifugation. Ag-Sb-Se nanocrystals are prone to the oxidation under ambient conditions or in thin films. Ag-Sb-Se nanocrystals, however, form long-term stable colloidal solutions in non-polar solvents, if stored under inert atmosphere.

Synthesis of Cu-Sb-Se nanocrystals. The CuSbSe₂ and Cu₃SbSe₄ nanocrystals were prepared in close analogy to the Ag-Sb-Se synthesis, explained above. CuCl and SbCl₃ were chosen as metal precursors, while Se precursor was kept the same. To prepare CuSbSe₂ nanocrystals, the following amounts of Cu, Sb, and Se precursors were introduced in the reaction mixture: 0.5 mmol of CuCl, 0.5 mmol of SbCl₃ and 1 mmol of Se. For the synthesis of Cu₃SbSe₄ nanocrystals, the amounts of Cu, Sb, and Se precursors were adjusted to 0.75 mmol of CuCl, 0.25 mmol of SbCl₃ and 0.75 mmol of Se. Reaction temperature was tuned between 80 and 150°C. At lower temperatures (and shorter reaction times), binary Cu_{2-x}Se byproducts were observed. Cu-Sb-Se nanocrystals were purified and stored in the glovebox.

Synthesis of AgBiSe₂ and CuBiSe₂ nanocrystals. The MBiSe₂ nanocrystals (where M is Ag or Cu) were synthesized at 120°C and 1 min reaction conditions. AgI (or CuCl) and BiCl₃ were chosen as metal precursors, while Se precursor was kept the same as for M-Sb-Se nanocrystals. MBiSe₂ nanocrystals were purified and stored in the glovebox.

Characterization. As-synthesized colloidal I-V-VI nanocrystals were characterized by transmission electron microscopy (size and size distribution; with JEM-1400 Plus JEOL), energy dispersive X-ray spectroscopy (composition quantification; with FEI Quanta 200 FEG), X-ray diffraction (crystal structure; with Rigaku SmartLab), photoluminescence (optical absorption; with Agilent Cary 5000). Composition quantifications were taken at 4-6 different regions, which enable higher precision (arithmetic mean)

and an error (standard deviation) for each quantified element. Optical band gaps were extracted from absorption spectra of stable colloidal solutions. To estimate absorption coefficients, thin films of I-V-VI nanocrystals were spin-coated on 20×20 mm glass substrates and cross-linked

with short-chain 1,2-ethanedithiol ligands (spin-coating the 0.1 vol.% of 1,2-ethanedithiol in acetonitrile). The thickness and continuity of thin films were measured by atomic force microscopy (AFM Agilent 5500). Absorption coefficients were calculated as previously published.²⁵

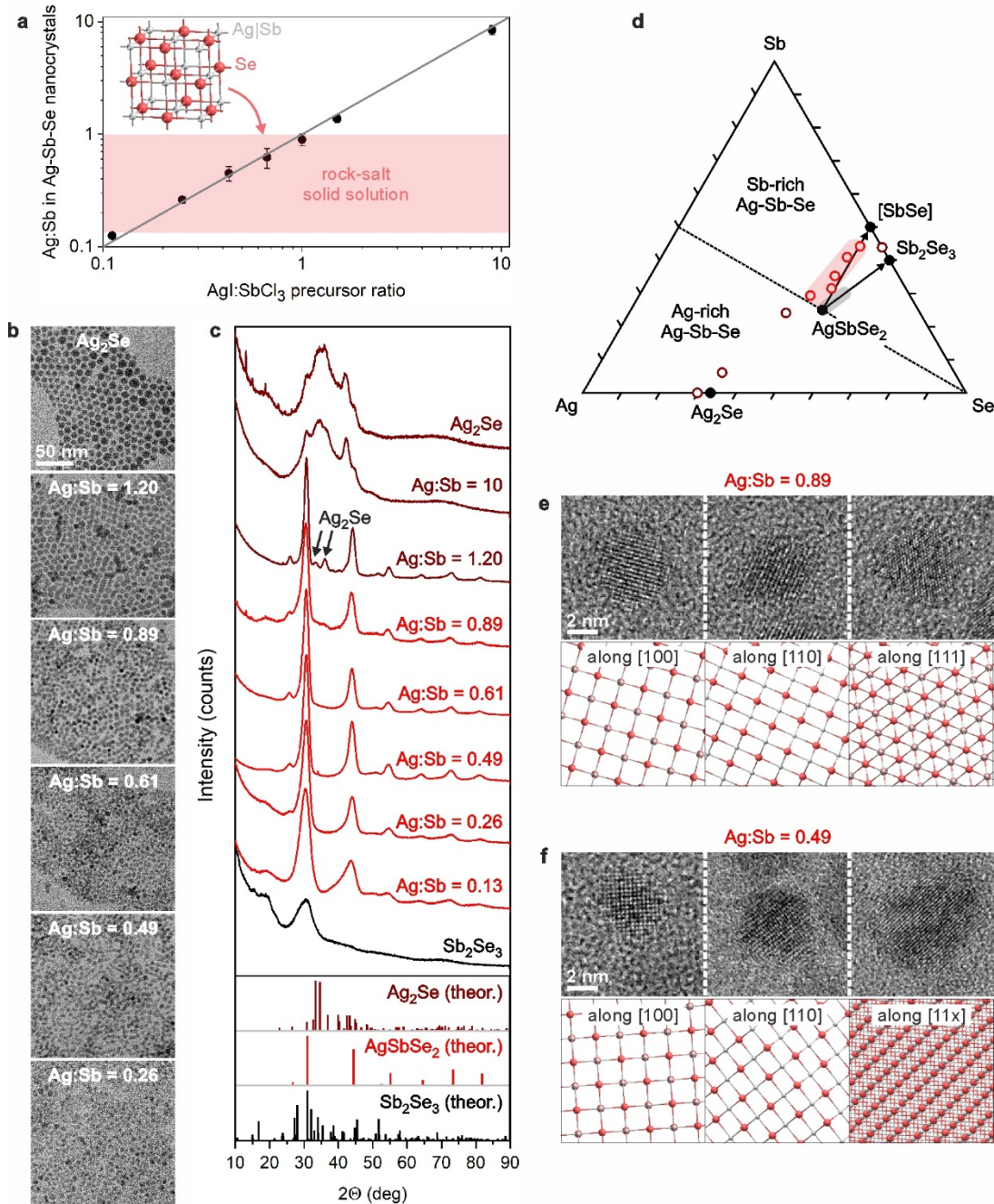


Figure 1. (a) Composition of Ag-Sb-Se nanocrystal samples as a function of molar ratio between initial metal halide precursors. The rock-salt solid solution for Ag-Sb-Se nanocrystals is highlighted. Inset (a): a unit cell of rock salt crystal structure of Ag-Sb-Se nanocrystals. (b) Transmission electron microscopy images and (c) X-ray diffractograms of nanocrystal samples, prepared using different molar ratios of AgI and SbCl₃, and otherwise same reaction conditions of $T_{\text{growth}} = 90^{\circ}\text{C}$ and $t_{\text{growth}} = 30$ min. Red color in (c) denotes single-phase Ag-Sb-Se rock-salt diffractograms; dark-red color in (c) denotes Ag₂Se or two-phase diffractograms. Simulated X-ray diffractograms are provided for comparison. (d) Ternary Ag-Sb-Se phase diagram, illustrating experimentally-achieved compositions of Ag-Sb-Se nanocrystals and rock-salt solid solution for bulk (shaded gray region) and for nanocrystals (shaded red region). Known compounds (Ag₂Se, AgSbSe₂, Sb₂Se₃) and 1:1 [SbSe] stoichiometry are show for convenience. Scale bar is 10 at.%. (e,f) High-resolution transmission electron microscopy images of Ag-Sb-Se nanocrystals with Ag-Sb atomic ratios of 0.89 and 0.49, and atomic reconstructions of viewed directions, corresponding to the rock salt crystal structure.

RESULTS AND DISCUSSIONS

Composition Control of Ag-Sb-Se Nanocrystals. We demonstrate that our synthetic protocol enables composition control by performing a series of syntheses at 90°C and 30 min of growth time using different ratios of metal halide salts. Using energy dispersive X-ray (EDX, **Figure S1**) spectroscopy, we determine the composition of Ag-Sb-Se nanocrystals and confirm that our reaction is nearly quantitative, i.e. the ratio of introduced AgI and SbCl₃ matches closely the ratio between Ag and Sb in obtained Ag-Sb-Se nanocrystals (**Figure 1a**). Transmission electron microscopy (TEM, **Figure 1b**) analysis shows that the size and size distribution of Ag-Sb-Se nanocrystals remains constant (5.3 ± 0.4 nm, 11-15% size distributions, **Figures S2** and **S3**) across the composition series, highlighting the well-balanced reactivity (i.e., co-precipitation) of Ag and Sb precursors in the reaction system.

X-ray diffraction measurements on the nanocrystal composition series reveal a broad solid solution for Sb-rich Ag-Sb-Se compositions (i.e., $x < y$ in $\text{Ag}_x\text{Sb}_y\text{Se}_z$, **Figure 1c**). Specifically, we find that Ag-Sb-Se nanocrystals with Ag:Sb atomic ratios between 0.89 and 0.13 exhibit cubic rock-salt structure (inset of **Figure 1a**). The Ag-rich Ag-Sb-Se compositions of nanocrystals (i.e., $x > y$ in $\text{Ag}_x\text{Sb}_y\text{Se}_z$) show a mixture of Ag₂Se and rock-salt AgSbSe₂ phases. These findings are in good correspondence with the bulk Ag-Sb-Se materials.²⁴ In particular, rock-salt solid solution is reported between AgSbSe₂ and Ag₂Sb₄Se₇ compositions, while there are no ternary compounds for the Ag-rich half of the Ag-Sb-Se phase diagram of bulk materials.²⁴ Mapping these rock-salt solid solutions on ternary diagram (**Figure 1d**) reveals clear differences between bulk and nanoscale Ag-Sb-Se materials. For bulk, the rock-salt solid solution lays on AgSbSe₂-Sb₂Se₃ phase equilibrium.²⁴ In contrast, Ag-Sb-Se nanocrystals belong to the solid solution between AgSbSe₂ and sub-stoichiometric Sb selenide (SbSe), and their composition can therefore be best described as $\text{Ag}_x\text{Sb}_{1-x}\text{Se}$. In addition, the $\text{Ag}_x\text{Sb}_{1-x}\text{Se}$ solid solution for nanocrystals spans wider range of Sb-rich Ag-Sb-Se compositions (nominally, from AgSbSe₂ to AgSb₈Se₉, **Figure 1d**).

High-resolution TEM measurements for two Ag-Sb-Se nanocrystal batches with distinctly different compositions (Ag:Sb ratio = 0.89, **Figure 1e** and Ag:Sb ratio = 0.49, **Figure 1f**) reveal the crystallographic orientations for the cubic rock salt structure type (e.g., [100], [110], and [111] viewing axes), thus proving the existence of rock-salt solid solution for Sb-rich Ag-Sb-Se compositions of nanocrystals (i.e., Ag:Sb < 1). The EDX quantifications and high-resolution TEM analysis (**Figures 1d-f**) align well with the change of lattice parameter, as extracted from X-ray diffractograms (**Figure S4**). Instead of lattice contraction towards Sb-rich side of Ag-Sb-Se solid solution (which would be a case for the AgSbSe₂-Sb₂Se₃ solid solution due to the cumulative effect of smaller ionic radius of Sb³⁺ than for Ag⁺ and increasing concentration of cationic vacancies),²⁶ here we

observe a slight expansion of Ag-Sb-Se lattice with increasing Sb content, being associated with larger covalent radius of Sb than for Ag and absence of vacancies in the $\text{Ag}_x\text{Sb}_{1-x}\text{Se}$ structure (inset of **Figure 1c**).²⁷

We noted from literature that while these sub-stoichiometric Sb chalcogenides are known for Sb-Te binary compounds SbTe and Sb₂Te (both of which exhibit closely related to the rock salt rhombohedral unit cells with octahedral coordination spheres for all Sb and Te atoms^{28,29}), they are not known for bulk Sb selenide materials.²⁴ The existence of AgSbSe₂-SbSe solid solution for nanocrystals can be associated with larger lattice constants as compared to the bulk AgSbSe₂ (i.e., geometrical reason, **Figure S4**) as well as with surface ligand passivation (i.e., a charge balance reason).

Finally, our methodology can also be applied to successfully prepare binary selenides, Ag₂Se and Sb₂Se₃, when one of elemental sources is omitted from the synthesis (**Figures 1b, 1c, and S5**). This emphasizes additionally an excellent composition control that we achieve for the entire region of Ag-Sb-Se materials.

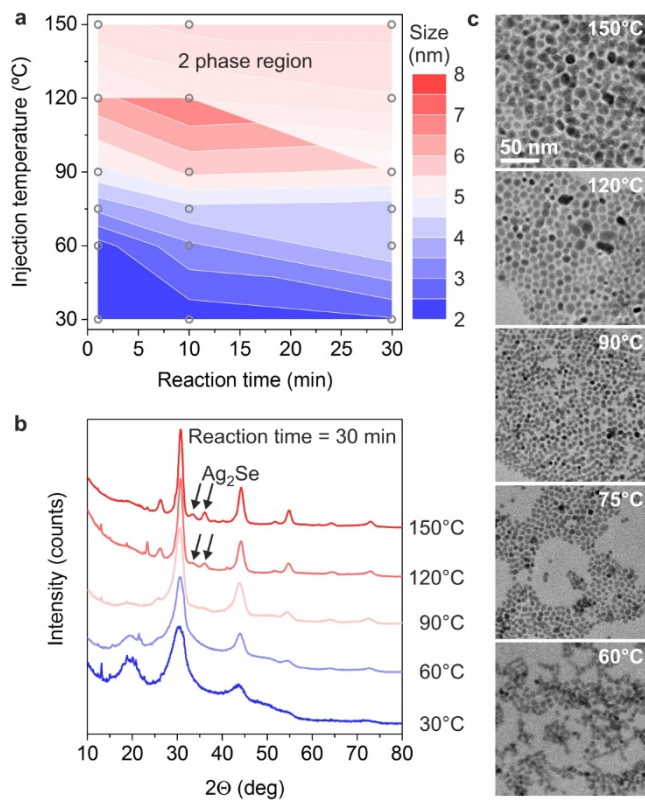


Figure 2. (a) A size map for AgSbSe₂ nanocrystals, plotted in coordinates of injection temperature and reaction time. The 2 phase region (Ag₂Se + AgSbSe₂) is shaded for clarity. (b,c) X-ray diffraction patterns and transmission electron microscopy images of nanocrystal samples, prepared at different reaction temperatures and otherwise same reaction conditions ($t_{\text{growth}} = 30$ min). The admixture of Ag₂Se binary material is observable at high reaction temperatures, $T_{\text{growth}} \geq 120^\circ\text{C}$.

Size Control of Ag-Sb-Se Nanocrystals. In order to study size control of Ag-Sb-Se nanocrystals, we systematically vary two reaction parameters: reaction temperature (between 30°C and 150°C) and reaction time (between 1 min and 30 min). We perform this parameter sweep for two compositions: one with an Ag:Sb ratio ≈ 1 (i.e., AgSbSe₂) and one Sb-rich with an Ag:Sb ratio ≈ 0.5 (i.e., AgSb₂Se₃). For both compositions, we find that nanocrystal size can be accurately adjusted between 2 and 7 nm by varying the injection temperature between 30°C and 90°C (**Figures 2a** and **S6**).

Figure 2a shows a size map for nanocrystals with nominal composition of AgSbSe₂ (i.e., Ag:Sb ratio ≈ 1), based on 18 samples. XRD data (width of Bragg reflections, **Figure 2b**) and TEM images (**Figure 2c**) indicate that the size of AgSbSe₂ nanocrystals increases proportionally to the reaction temperature. This can be explained by increasing growth rates for nanocrystals at higher growth temperatures, as is typical for various syntheses of colloidal nanocrystals.^{17, 30}

Due to high reactivity of elemental Se precursor in 1:1 oleylamine:dodecanethiol mixture, formation of ultrasmall AgSbSe₂ nanocrystals is possible even at room temperature (**Figures 2a** and **2b**). As explained previously,³¹ dodecanethiol-induced reduction of Se leads to the formation of oleylammonium-(poly)selenides, which exhibit notably higher reactivity than Se powders or alkylphosphine adducts. While reaction temperatures lower than 90°C yield pure phase and narrow size distribution AgSbSe₂ nanocrystals, at high temperatures, we observe an AgSbSe₂ and Ag₂Se admixture as well as broad size distributions of nanocrystals (**Figures 2b** and **2c**). The formation of Ag₂Se byproducts at high reaction temperatures is in agreement with previous publication, where it is associated with slow incorporation of Sb salt in the Ag-Sb-Se structure, as compared to Ag precursor.¹⁷ Large size distributions can be linked to Ostwald ripening growth processes at high reaction temperatures. Reaction time plays a relatively minor role on the resulting size and size distribution of AgSbSe₂.

nanocrystals, which can be explained by the fast, quantitative reaction (**Figure 1c**) followed by generally slow Ostwald ripening growth at low temperatures (such as 30–90°C).

We observe very similar results for Sb-rich Ag-Sb-Se nanocrystals with nominal composition of AgSb₂Se₃ (**Figure S6**). In analogy to AgSbSe₂ nanocrystals, the size of AgSb₂Se₃ nanocrystals is defined mainly by the injection temperature, while reaction time has a minor effect. The phase-pure rock-salt crystal structure of AgSb₂Se₃ nanocrystals is only retained at low reaction temperatures (from 30°C up to 110–120°C), above which binary Ag₂Se byproduct forms.

We notice a qualitatively different X-ray diffraction pattern for AgSb₂Se₃ nanocrystals prepared at room temperature (**Figure S6b**). Abnormal broadening of the second Bragg reflection may point to the lack of crystallinity (i.e., amorphous structure) in these AgSb₂Se₃ nanocrystals, which could be leveraged for example for crystallization-exploiting phase-change memory applications.^{7, 32}

Finally, it is important to note that we estimate the size of AgSbSe₂ and AgSb₂Se₃ nanocrystals from the broadening of X-ray peaks (using Scherrer formula, **Figures 2** and **S6**). For the same samples, size evaluation from TEM images reveals systematically larger sizes by 1–2 nm (**Figure S7**). This observation suggests that Ag-Sb-Se nanocrystals are surrounded by thin sub-nm oxide shell, which is consistent with the facile oxidation of these ternary nanocrystalline materials (more details in the **Experimental Section**).

Beyond Ag-Sb-Se: Ag-Bi-Se, Cu-Sb-Se, and Cu-Bi-Se Nanocrystals. Having understood the Ag-Sb-Se system, we expand this synthetic protocol to other I-V-VI colloidal nanocrystals. We use the same selenium precursor, temperature range, and reaction times, while replacing Ag and/or Sb elemental sources with analogous metal halide salts of Cu and Bi, namely CuCl and BiCl₃. The results are summarized in **Figure 3**. Small-size AgBiSe₂ and CuBiSe₂ nanocrystals can be prepared at 120°C and short reaction times of 0.5–1 min (**Figures 3a** and **3b**).

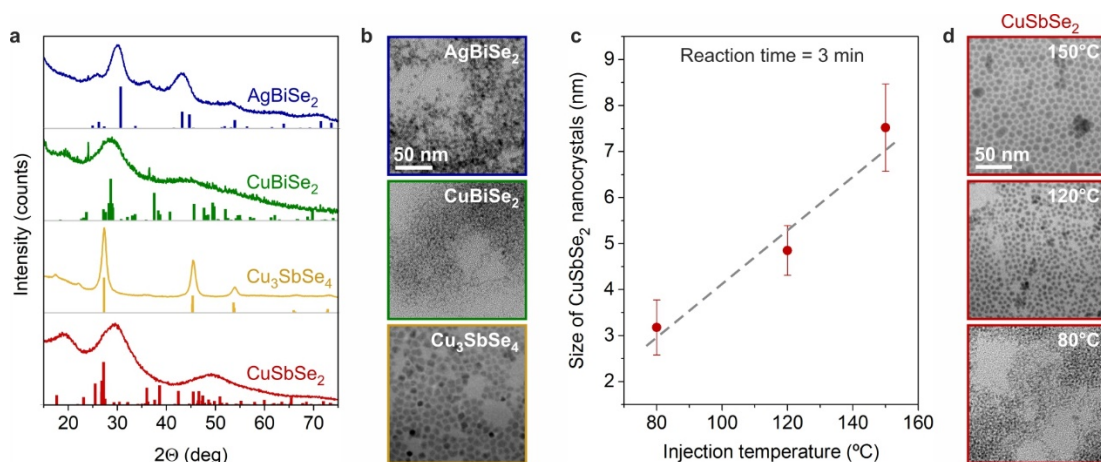


Figure 3. (a) X-ray diffraction patterns and (b) transmission electron microscopy images of various I-V-VI nanocrystals, prepared analogously to the Ag-Sb-Se nanocrystals. (c) Different sizes of CuSbSe₂ nanocrystals, prepared at injection temperatures between 80 and 150°C. (d) Transmission electron microscopy images of CuSbSe₂ nanocrystals, shown in panel (c).

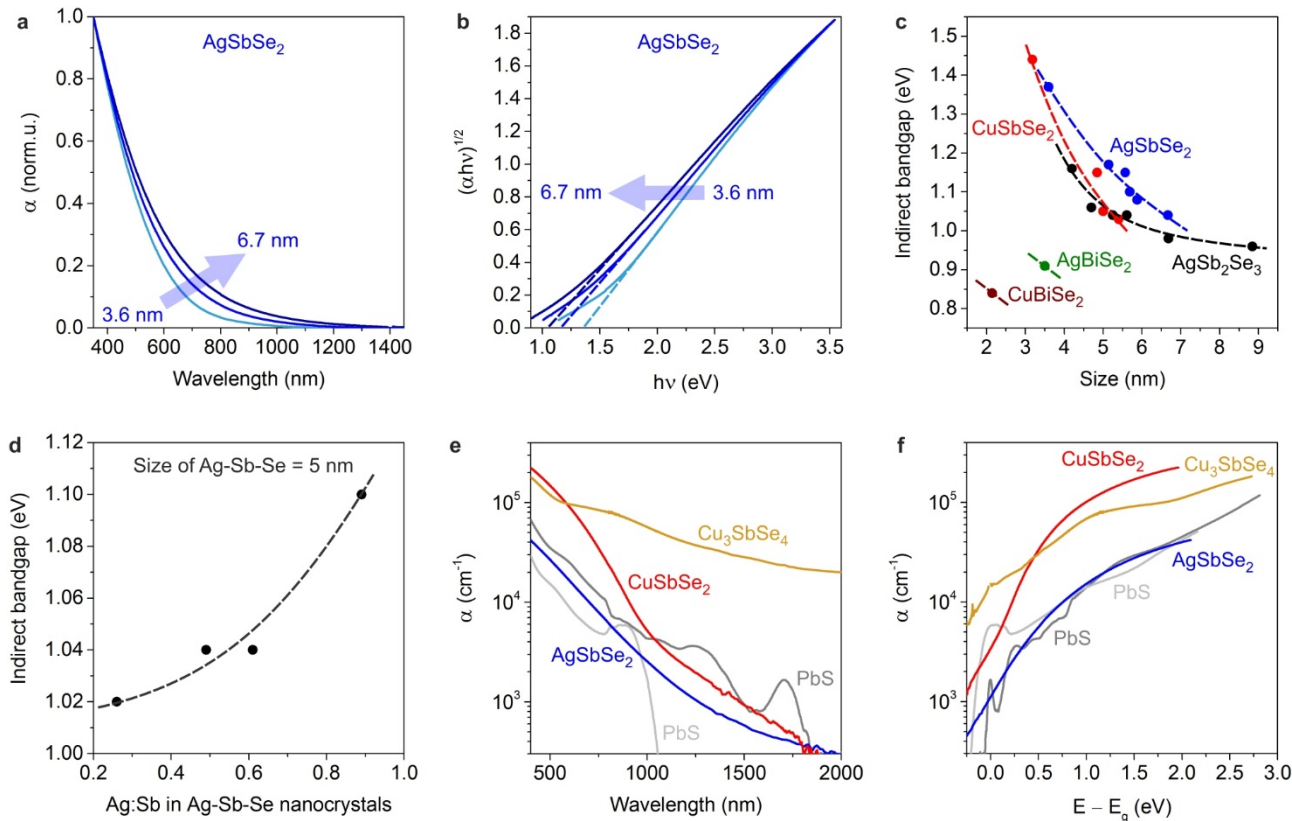


Figure 4. (a) Normalized absorption spectra of AgSbSe₂ nanocrystals, having different sizes between 3.6 and 6.7 nm. (b) Tauc analysis of absorption spectra, shown in panel (a). (c) Size-dependent indirect band gap of various I-V-VI nanocrystals, as extracted from Tauc plots. (d) Composition-dependent indirect band gap of Ag-Sb-Se nanocrystals, 5 nm in diameter. (e,f) Absorption coefficients of thin films for various I-V-VI nanocrystals, shown in comparison with two sizes of PbS nanocrystals.

For the Cu-Sb-Se system, we achieve two compositions, matching the stoichiometries of ternary compounds in the bulk, CuSbSe₂ and Cu₃SbSe₄ (Figures 3a-3d). The reaction works similarly to the Ag-Sb-Se nanocrystals. The composition control can be attained by adjusting the ratio between metal halide precursors, and the size of nanocrystals can be tuned by adjusting the reaction temperature (Figures 3c and 3d). However, in contrast to the Ag-Sb-Se nanocrystals, for Cu-containing I-V-VI nanocrystals (e.g., Cu-Sb-Se materials), we do not observe a 2-phase region at higher reaction temperatures. In fact, pure-phase Cu-Sb-Se nanocrystals can be synthesized at higher reaction temperatures of 120-150°C, while for lower temperatures (and shorter reaction times) we observe the Cu_{2-x}Se admixture, as manifested by infrared plasmonic feature³³ on absorption spectra (Figure S8). These observations suggest kinetic differences between Cu and Ag halides in this reaction system, such as smaller activation energy for CuCl conversion, but large reactivity difference between CuCl and SbCl₃ at lower temperatures (in contrast, a well-balanced reactivity between AgI and SbCl₃ is expected at low temperatures as well as bigger activation energy for the AgI conversion). Figure S9 illustrates these conclusions schematically.

X-ray diffractograms of obtained I-V-VI nanocrystals (Figure 3a) correspond well to expected bulk structures (Figure S10).³⁴⁻³⁷ Low lattice symmetry of CuBiSe₂ and CuSbSe₂ compounds^{36, 37} and line broadening of Bragg reflections result in only broad features on X-ray diffraction patterns. The X-ray diffractograms AgBiSe₂ and Cu₃SbSe₄ nanocrystals match well to theoretical patterns of rhombohedral AgBiSe₂ and tetrahedral Cu₃SbSe₄ bulk compounds.^{34, 35}

Optical Properties of I-V-VI Nanocrystals. One property of I-V-VI material is their high absorption coefficients.^{2, 3} I-V-VI materials have narrow band gaps,¹⁶ making them of interest for infrared applications. Here, we therefore analyze absorption spectra of various I-V-VI nanocrystals as a function of size and composition of I-V-VI nanocrystals.

Figure 4a shows the size-dependent absorption for three sizes of AgSbSe₂ nanocrystals, spanning from 3.6 to 6.7 nm. A clear red shift of absorption spectrum is observed with increasing nanocrystal size. To estimate the optical band gap of AgSbSe₂ nanocrystals, we employ Tauc analysis,³⁸ according to which, an indirect optical band gap can be extracted from Tauc plots in coordinates $(\alpha h\nu)^{0.5}$ vs. $h\nu$ by extrapolating a linear region to 0 (Figure 4b). Extracted indirect band gaps of AgSbSe₂ nanocrystals lay between 1.05-1.35 eV (Figure S11), which is larger than the indirect band

gap of bulk AgSbSe₂ (0.7 eV).⁴ This observation indicates the quantum-confinement regime in small 2-7 nm in size AgSbSe₂ nanocrystals. In accordance, the band gap of AgSbSe₂ nanocrystals increases with decreasing the nanocrystal size (**Figure 4c**). Similarly, we observe a size-dependent, indirect band gap for AgSb₂Se₃ and CuSbSe₂ nanocrystals (**Figures 4c** and **S12-13**), which are also larger than bulk band gaps (e.g., $E_{\text{CuSbSe}_2}^{\text{bulk}} = 1.04$ eV).²

Comparison of the size dependences for AgSbSe₂ and AgSb₂Se₃ nanocrystals reveals a noticeable composition effect. In particular, the indirect band gap is systematically smaller for AgSb₂Se₃ nanocrystals than for stoichiometric AgSbSe₂ nanocrystals by about 50-100 meV (**Figure 4c**). We hypothesize that this can be attributed to large concentration of antisite defects (i.e., Sb_{Se}, Ag_{Se}, Sb_{Ag}, etc.) and higher concentration of valent electrons, which lead to the filling of shallow in-gap trap states and thus band gap narrowing. Optical band gap becomes even narrower for highly Sb-rich Ag-Sb-Se nanocrystals, supporting our hypothesis (**Figure 4d**). Another composition effect can be observed when comparing Sb- and Bi-containing I-V-VI nanocrystals. In particular, small-size CuBiSe₂ and AgBiSe₂ nanocrystals exhibit narrower optical band gaps than their Sb-containing counterparts (**Figures 4c** and **S14**), the trend observed also for bulk I-V-VI materials.³ Expectably, small-size I-Bi-VI nanocrystals exhibit larger band gaps than their bulk counterparts (e.g., $E_{\text{AgBiSe}_2}^{\text{bulk}} = 0.6$ eV),⁵ due to quantum-confinement effects.

Finally, we measure absorption coefficients of thin films of I-V-VI nanocrystals (**Figure 4e**). We observe high absorption coefficients on the order of 10⁵ cm⁻¹. Comparing the absorptivity with that of PbS nanocrystals (**Figure 4e**), we find that AgSbSe₂ and CuSbSe₂ thin films exhibit absorption coefficients similar to the PbS thin films in the near-infrared and visible spectral regions, making I-V-VI nanocrystals a suitable lead-free alternative to explore.

Thin films of Cu₃SbSe₄ nanocrystals are much more absorptive than PbS. The Cu₃SbSe₄ material is direct band gap semiconductor with very narrow band gap between 100 and 400 meV in the bulk (which is even narrower when atomic defects or dopants are introduced).¹⁸ Our analysis of thin film absorption allows us to estimate the direct band gap of 7.6 nm Cu₃SbSe₄ nanocrystals to be 320 meV (**Figure S15**). We also note that absorptivity of I-V-VI nanocrystals remains high at the estimated band gap values (**Figures S11-15**). This can be associated with notable amount of in-gap defect states e.g. due to disorder of cations or presence of atomic vacancies.

A further comparison of absorptivities can be made by plotting absorption vs. the photon energy minus the optical band gap, E_g (**Figure 4f**). Such comparison clearly illustrates the benefit of I-V-VI semiconductors as efficient absorbers in infrared and visible spectral region.

CONCLUSIONS

This paper reports the first synthesis of small sub-10 nm I-V-VI selenide nanocrystals in form of stable colloids. We focus on Ag-Sb-Se material and achieve accurate size and composition control as well as narrow size distributions for Ag-Sb-Se nanocrystals. We then show that this synthetic approach can be extended to prepare other small-size I-V-VI colloidal nanocrystals, such as CuSbSe₂, Cu₃SbSe₄, AgBiSe₂, and CuBiSe₂. With this library of colloidal I-V-VI nanocrystals, we study their size and composition-dependent optical properties. Some of the I-V-VI nanocrystals exhibit very high absorption coefficients, making them promising non-Cd, Pb, or Hg containing materials for near- and mid-infrared applications.

ASSOCIATED CONTENT

Supporting data to the article (**Figures S1-S15**), containing quantifications of EDX spectra, extraction of lattice constants, TEM images, size distributions and additional XRD patterns for Ag-Sb-Se nanocrystals; crystal structure of Cu₃SbSe₄; absorption spectra and Tauc analysis of various I-V-VI nanocrystals. This material is available free of charge via the Internet at <http://pubs.acs.org>.

AUTHOR INFORMATION

Corresponding Author

* vwood@ethz.ch

Author Contributions

The manuscript was written through contributions of all authors.

Funding Sources

This work was financially supported by the BASF in frame of Joint Research Network on Advanced Materials and Systems (JONAS) and by the Swiss National Science foundation via a research grant (No. 175889), NCCR "QSIT – Quantum Science and Technology", and an Ambizione Fellowship (No. 161249).

ACKNOWLEDGMENT

Authors acknowledge Dr. Bernd Bruchmann, Head of JONAS Research Network, for support and discussions. Authors thank to Mario Mücklich for technical assistance. TEM and EDX measurements were performed at the Scientific Center for Optical and Electron Microscopy (ScopeM) of the Swiss Federal Institute of Technology.

REFERENCES

1. Peccerillo, E.; Durose, K., Copper-antimony and copper-bismuth chalcogenides - Research opportunities and review for solar photovoltaics. *MRS Energy Sustain.* **2018**, *5*, E13.
2. Xue, D.-J.; Yang, B.; Yuan, Z.-K.; Wang, G.; Liu, X.; Zhou, Y.; Hu, L.; Pan, D.; Chen, S.; Tang, J., CuSbSe₂ as a Potential Photovoltaic Absorber Material: Studies from Theory to Experiment. *Adv. Energy Mater.* **2015**, *5*, 1501203.

3. Yu, L.; Kokenyesi, R. S.; Keszler, D. A.; Zunger, A., Inverse Design of High Absorption Thin-Film Photovoltaic Materials. *Adv. Energy Mater.* **2013**, *3*, 43-48.
4. Guin, S. N.; Chatterjee, A.; Negi, D. S.; Datta, R.; Biswas, K., High thermoelectric performance in tellurium free p-type AgSbSe₂. *Energy Environ. Sci.* **2013**, *6*, 2603-2608.
5. Guin, S. N.; Srihari, V.; Biswas, K., Promising thermoelectric performance in n-type AgBiSe₂: effect of aliovalent anion doping. *J. Mater. Chem. A* **2015**, *3*, 648-655.
6. Du, B.; Li, H.; Xu, J.; Tang, X.; Uher, C., Enhanced Figure-of-Merit in Se-Doped p-Type AgSbTe₂ Thermoelectric Compound. *Chem. Mater.* **2010**, *22*, 5521-5527.
7. Wang, K.; Steimer, C.; Detemple, R.; Wamwangi, D.; Wuttig, M., Assessment of Se based phase change alloy as a candidate for non-volatile electronic memory applications. *Appl. Phys. A* **2005**, *81*, 1601-1605.
8. Morelli, D. T.; Jovovic, V.; Heremans, J. P., Intrinsically Minimal Thermal Conductivity in Cubic I-V-VI₂ Semiconductors. *Phys. Rev. Lett.* **2008**, *101*, 035901.
9. Samanta, M.; Roychowdhury, S.; Ghatak, J.; Perumal, S.; Biswas, K., Ultrahigh Average Thermoelectric Figure of Merit, Low Lattice Thermal Conductivity and Enhanced Microhardness in Nanostructured (GeTe)_x(AgSbSe₂)_{100-x}. *Chem. Eur. J.* **2017**, *23*, 7438-7443.
10. Guin, S. N.; Chatterjee, A.; Biswas, K., Enhanced thermoelectric performance in p-type AgSbSe₂ by Cd-doping. *RSC Adv.* **2014**, *4*, 11811-11815.
11. Quarez, E.; Hsu, K.-F.; Pcionek, R.; Frangis, N.; Polychroniadis, E. K.; Kanatzidis, M. G., Nanostructuring, Compositional Fluctuations, and Atomic Ordering in the Thermoelectric Materials AgPb_mSbTe_{2+m}. The Myth of Solid Solutions. *J. Am. Chem. Soc.* **2005**, *127*, 9177-9190.
12. Yarema, O.; Yarema, M.; Wood, V., Tuning the Composition of Multicomponent Semiconductor Nanocrystals: The Case of I-III-VI Materials. *Chem. Mater.* **2018**, *30*, 1446-1461.
13. Norris, D. J.; Bawendi, M. G., Measurement and assignment of the size-dependent optical spectrum in CdSe quantum dots. *Phys. Rev. B* **1996**, *53*, 16338-16346.
14. Yarema, O.; Yarema, M.; Bozyigit, D.; Lin, W. M. M.; Wood, V., Independent Composition and Size Control for Highly Luminescent Indium-Rich Silver Indium Selenide Nanocrystals. *ACS Nano* **2015**, *9*, 11134-11142.
15. Yarema, O.; Yarema, M.; Lin, W. M. M.; Wood, V., Cu-In-Te and Ag-In-Te colloidal nanocrystals with tunable composition and size. *Chem. Commun.* **2016**, *52*, 10878-10881.
16. Bernechea, M.; Miller, N. C.; Xercavins, G.; So, D.; Stavriniadis, A.; Konstantatos, G., Solution-processed solar cells based on environmentally friendly AgBiS₂ nanocrystals. *Nat. Photonics* **2016**, *10*, 521.
17. Liu, Y.; Cadavid, D.; Ibáñez, M.; De Roo, J.; Ortega, S.; Dobrozhan, O.; V. Kovalenko, M.; Cabot, A., Colloidal AgSbSe₂ nanocrystals: surface analysis, electronic doping and processing into thermoelectric nanomaterials. *J. Mater. Chem. C* **2016**, *4*, 4756-4762.
18. Liu, Y.; García, G.; Ortega, S.; Cadavid, D.; Palacios, P.; Lu, J.; Ibáñez, M.; Xi, L.; De Roo, J.; López, A. M.; Martí-Sánchez, S.; Cabezas, I.; Mata, M. d. I.; Luo, Z.; Dun, C.; Dobrozhan, O.; Carroll, D. L.; Zhang, W.; Martins, J.; Kovalenko, M. V.; Arbiol, J.; Noriega, G.; Song, J.; Wahnón, P.; Cabot, A., Solution-based synthesis and processing of Sn- and Bi-doped Cu₃SbSe₄ nanocrystals, nanomaterials and ring-shaped thermoelectric generators. *J. Mater. Chem. A* **2017**, *5*, 2592-2602.
19. Chen, C.; Qiu, X.; Ji, S.; Jia, C.; Ye, C., The synthesis of monodispersed AgBiS₂ quantum dots with a giant dielectric constant. *Cryst. Eng. Comm.* **2013**, *15*, 7644-7648.
20. Zhou, B.; Li, M.; Wu, Y.; Yang, C.; Zhang, W.-H.; Li, C., Monodisperse AgSbS₂ Nanocrystals: Size-Control Strategy, Large-Scale Synthesis, and Photoelectrochemistry. *Chem. Eur. J.* **2015**, *21*, 1143-1151.
21. Guria, A. K.; Prusty, G.; Chacrabarty, S.; Pradhan, N., Fixed Aspect Ratio Rod-to-Rod Conversion and Localized Surface Plasmon Resonance in Semiconducting I-V-VI Nanorods. *Adv. Mater.* **2016**, *28*, 447-453.
22. Das, A.; Hsu, B.; Shamirian, A.; Yang, Z.; Snee, P. T., Synthesis of High-Quality AgSbSe₂ and AgBiSe₂ Nanocrystals with Antimony and Bismuth Silylamide Reagents. *Chem. Mater.* **2017**, *29*, 4597-4602.
23. Liu, Y.; Yang, J.; Gu, E.; Cao, T.; Su, Z.; Jiang, L.; Yan, C.; Hao, X.; Liu, F.; Liu, Y., Colloidal synthesis and characterisation of Cu₃SbSe₃ nanocrystals. *J. Mater. Chem. A* **2014**, *2*, 6363-6367.
24. Boutserrit, A.; Ollitrault-Fichet, R.; Rivet, J.; Dugué, J., Description du système ternaire Ag-Sb-Se. *J. Alloys Compd.* **1993**, *191*, 223-232.
25. Cesaria, M.; Caricato, A. P.; Martino, M., Realistic absorption coefficient of ultrathin films. *J. Opt.* **2012**, *14*, 105701.
26. Shannon, R., Revised effective ionic radii and systematic studies of interatomic distances in halides and chalcogenides. *Acta Crystallogr. A* **1976**, *32*, 751-767.
27. Pyykkö, P.; Atsumi, M., Molecular Single-Bond Covalent Radii for Elements 1-118. *Chem. Eur. J.* **2009**, *15*, 186-197.
28. Agafonov, V.; Rodier, N.; Ceolin, R.; Bellissent, R.; Bergman, C.; Gaspard, J. P., Structure of Sb₂Te. *Acta Crystallogr. C* **1991**, *47*, 1141-1143.
29. Stasova, M. M., Crystal structure of bismuth selenides and bismuth and antimony tellurides. *J. Struct. Chem.* **1967**, *8*, 584-589.
30. Yarema, O.; Bozyigit, D.; Rousseau, I.; Nowack, L.; Yarema, M.; Heiss, W.; Wood, V., Highly luminescent, size- and shape-tunable copper indium selenide based colloidal nanocrystals. *Chem. Mater.* **2013**, *25*, 3753-3757.
31. Liu, Y.; Yao, D.; Shen, L.; Zhang, H.; Zhang, X.; Yang, B., Alkylthiol-Enabled Se Powder Dissolution in Oleylamine at Room Temperature for the Phosphine-Free Synthesis of Copper-Based Quaternary Selenide Nanocrystals. *J. Am. Chem. Soc.* **2012**, *134*, 7207-7210.
32. Wuttig, M.; Yamada, N., Phase-change materials for re-writeable data storage. *Nat. Mater.* **2007**, *6*, 824.
33. Dorfs, D.; Härtling, T.; Miszta, K.; Bigall, N. C.; Kim, M. R.; Genovese, A.; Falqui, A.; Povia, M.; Manna, L., Reversible Tunability of the Near-Infrared Valence Band Plasmon Resonance in Cu_{2-x}Se Nanocrystals. *J. Am. Chem. Soc.* **2011**, *133*, 11175-11180.
34. Banas, M.; Atkin, D.; Bowles, J.; Simpson, P., Further Studies of Bohdanowiczite (AgBiSe₂) and Some Associated Minerals. *Bull. Mineral.* **1980**, *103*, 107-112.
35. Pfitzner, A., Crystal structure of tricopper tetraselenoantimonate (V), Cu₃SbSe₄. In *Z. Kristallogr.* **1994**, *209*, 685.
36. Förster, H.-J.; Bindi, L.; Stanley, C. J., Grundmannite, CuBiSe₂, the Se-analogue of emplectite, a new mineral from the El Dragón mine, Potosí, Bolivia. *Eur. J. Mineral.* **2016**, *28*, 467-477.
37. Zhou, J.; Bian, G.-Q.; Zhu, Q.-Y.; Zhang, Y.; Li, C.-Y.; Dai, J., Solvothermal crystal growth of CuSbQ₂ (Q = S, Se) and the correlation between macroscopic morphology and microscopic structure. *J. Solid State Chem.* **2009**, *182*, 259-264.
38. Tauc, J.; Grigorovici, R.; Vancu, A., Optical Properties and Electronic Structure of Amorphous Germanium. *Phys. Status Solidi B* **1966**, *15*, 627-637.

Supporting Information for
Composition and size controlled I-V-VI semiconductor nanocrystals

Olesya Yarema,[†] Maksym Yarema,[†] Annina Moser,[†] Olivier Enger,[‡] and Vanessa Wood^{†,*}

[†] Materials and Device Engineering Group, Department of Information Technology and Electrical Engineering, ETH Zurich,
CH-8092 Zurich, Switzerland

[‡] BASF Switzerland AG, Klybeckstrasse 141, CH-4057 Basel, Switzerland

vwood@ethz.ch

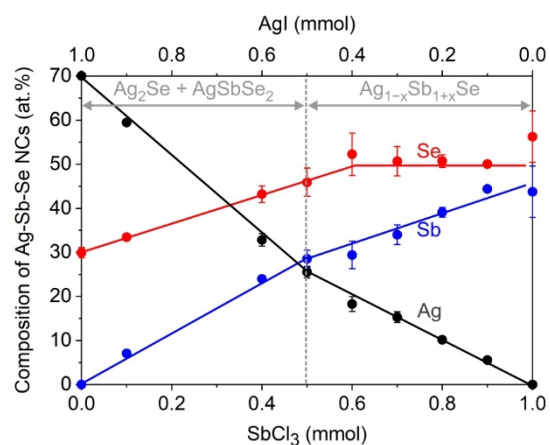


Figure S1. Energy dispersive X-ray (EDX) quantifications of Ag-Sb-Se nanocrystal samples, presented as a function of amounts of initial metal halide salts. Dashed vertical line demarcates the two-phase region ($\text{Ag}_2\text{Se} + \text{AgSbSe}_2$) and the $\text{Ag}_{1-x}\text{Sb}_{1+x}\text{Se}$ solid solution.

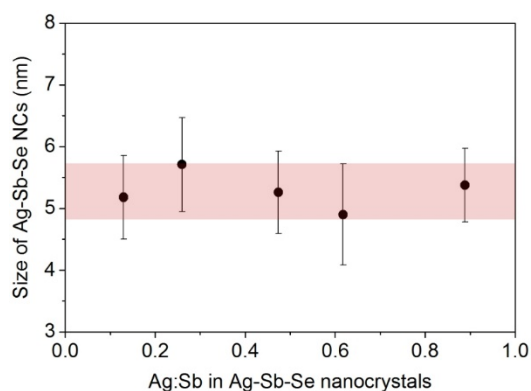


Figure S2. An average size of $\text{Ag}_{1-x}\text{Sb}_{1+x}\text{Se}$ nanocrystals, prepared at 90°C during 30 min (variable $\text{AgI}:\text{SbCl}_3$ molar ratio).

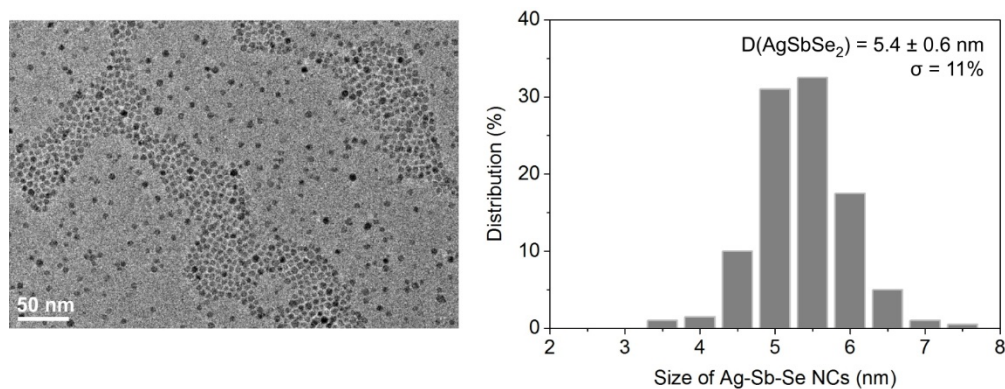


Figure S3. Transmission electron microscopy image and size distribution histogram of AgSbSe_2 nanocrystals, prepared at 90°C during 30 min.

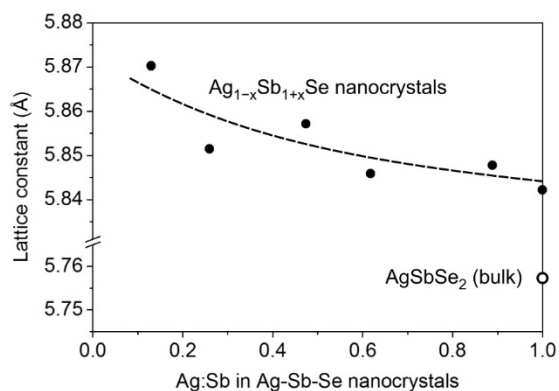


Figure S4. A lattice constant of rock salt structure of $\text{Ag}_{1-x}\text{Sb}_{1+x}\text{Se}$ nanocrystals, as calculated from the peak position of (002) Bragg reflection on X-ray diffractograms.

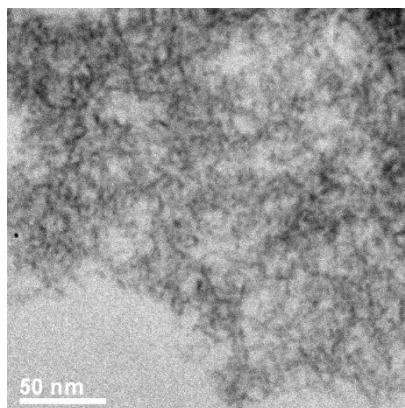


Figure S5. Transmission electron microscopy images of Sb_2Se_3 nanocrystals, prepared at $T_{\text{growth}} = 90^\circ\text{C}$ and $t_{\text{growth}} = 30$ min

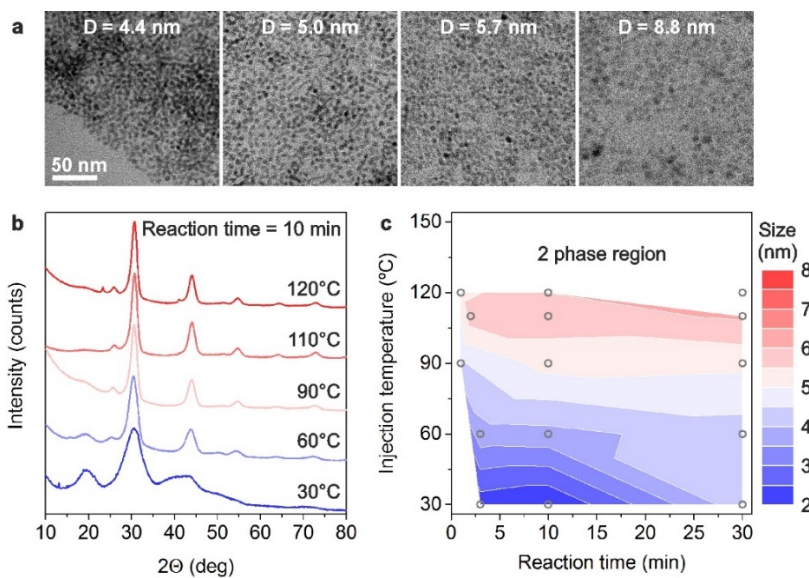


Figure S6. (a) Exemplar transmission electron microscopy images of AgSb_2Se_3 nanocrystals. (b) X-ray diffractograms of AgSb_2Se_3 nanocrystals, prepared at different temperatures, but otherwise same reaction conditions. (c) A size map for AgSb_2Se_3 nanocrystals in coordinated of injection temperature and reaction time.

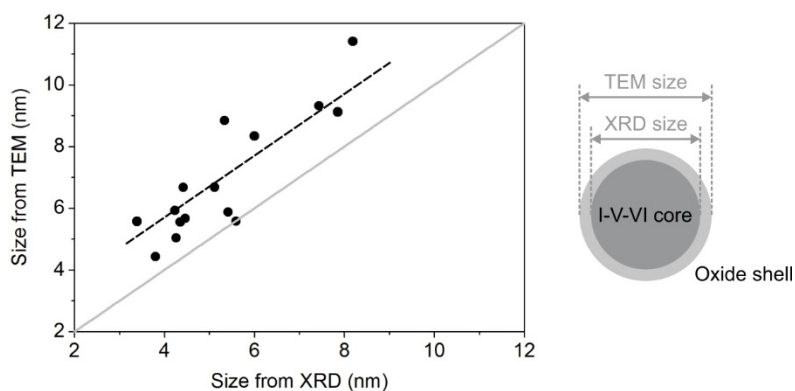


Figure S7. Average sizes of $\text{Ag}_{1-x}\text{Sb}_{1+x}\text{Se}$ nanocrystals, extracted from transmission electron microscopy images and X-ray diffractograms (Scherrer formula), and schematics of extracted sizes.

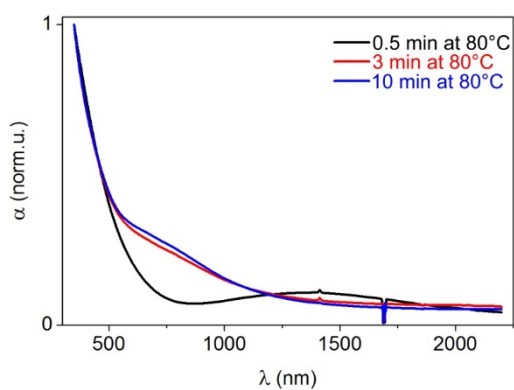


Figure S8. Absorption spectra of Cu_3SbSe_4 nanocrystals, synthesized at 80°C and different reaction times. Plasmonic feature, peaking at 1400 nm, indicates the presence of Cu_{2-x}Se binary byproduct.

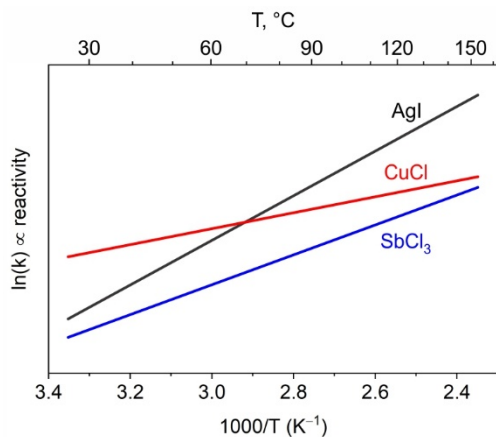


Figure S9. Arrhenius plot, illustrating reactivity of metal halides in the synthesis of I-V-VI colloidal nanocrystals, qualitatively.

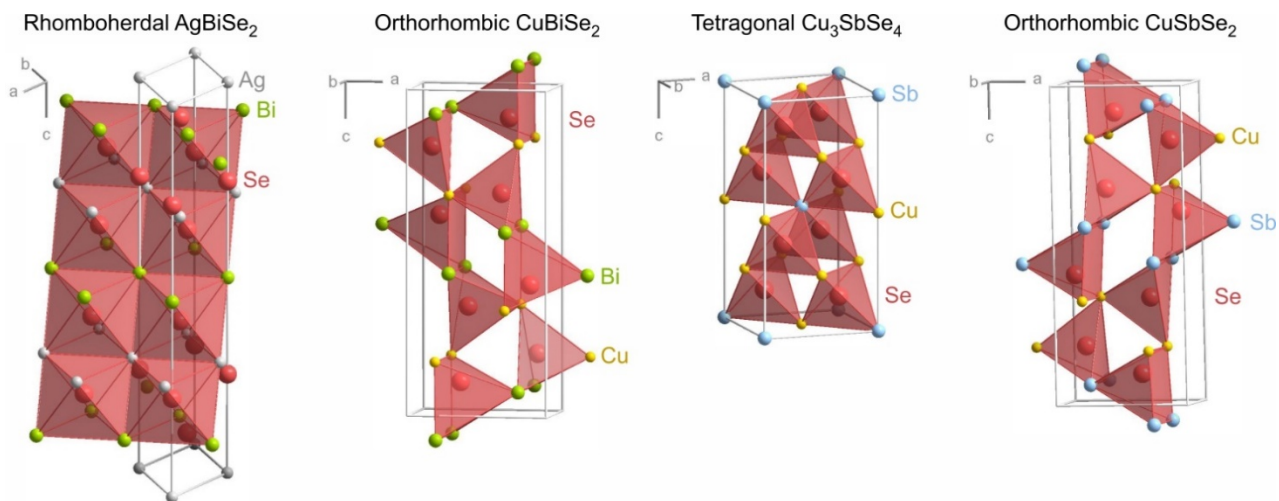


Figure S10. Crystal structures of bulk AgBiSe_2 , CuBiSe_2 , Cu_3SbSe_4 , and CuSbSe_2 semiconductor materials, indicating the atomic arrangements as arrays of Se polyhedra. AgBiSe_2 belongs to rhombohedral crystal system and can be seen as distorted rock-salt structure (see **Figure 1a**, inset), having a space-filling arrangement of Se octahedra. Cu_3SbSe_4 structure belongs to a family of tetrahedral semiconductors, in which all atoms have a coordination number of 4 (the other examples being e.g., zinc blende, chalcopyrite, III-V semiconductors, etc.). The structures of CuBiSe_2 and CuSbSe_2 are similar, exhibiting low-symmetry orthorhombic lattices, formed from distorted tetrahedra and tetragonal prisms. This non-conventional coordination environment for Se atoms can be explained by the fact that Sb and Bi typically have coordination numbers of 5, whereas Cu atoms remain tetrahedrally coordinated.

AgSbSe₂ nanocrystals

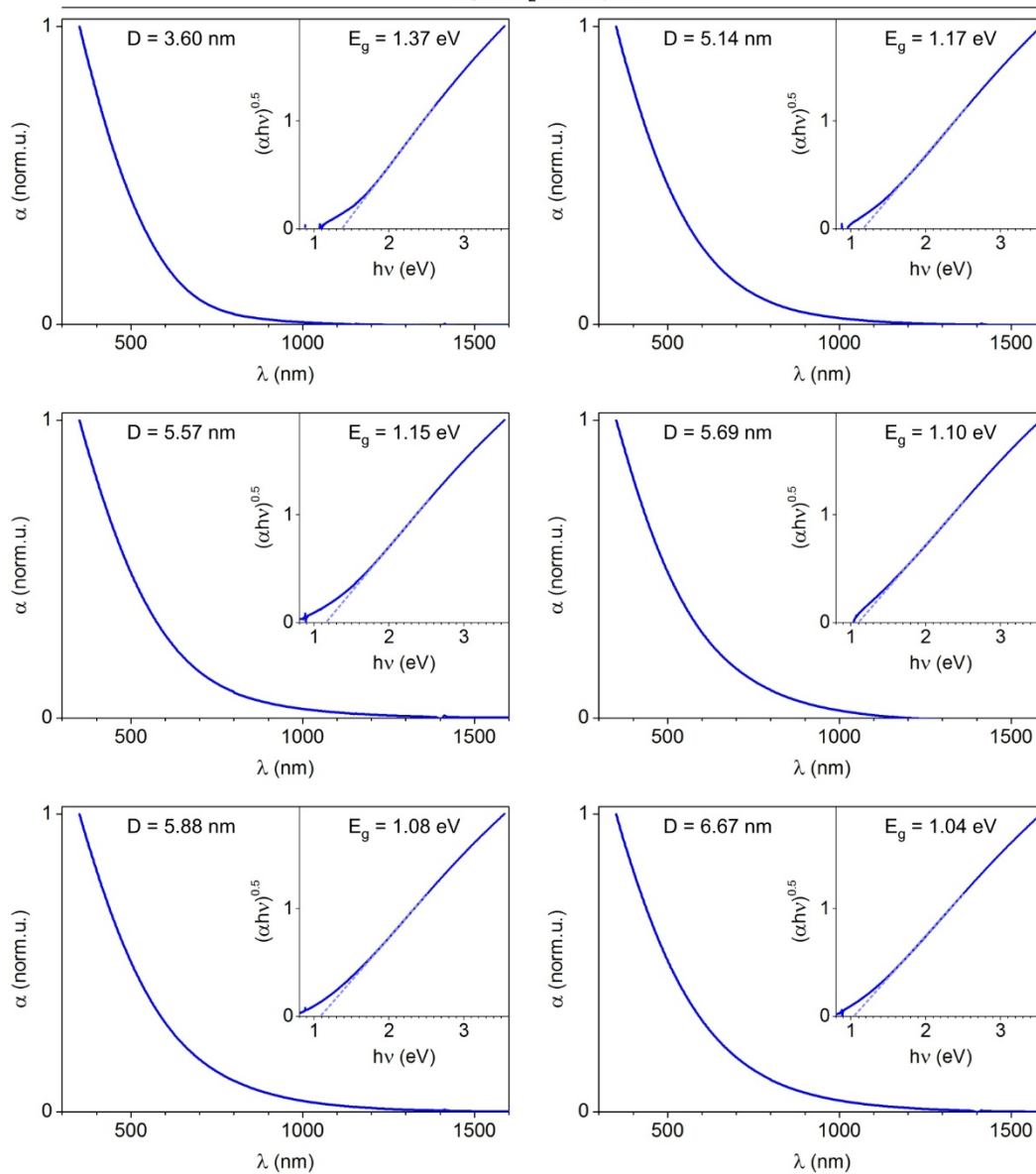


Figure S11. Absorption spectra and Tauc plots for AgSbSe₂ nanocrystals with different average sizes.

AgSb₂Se₃ nanocrystals

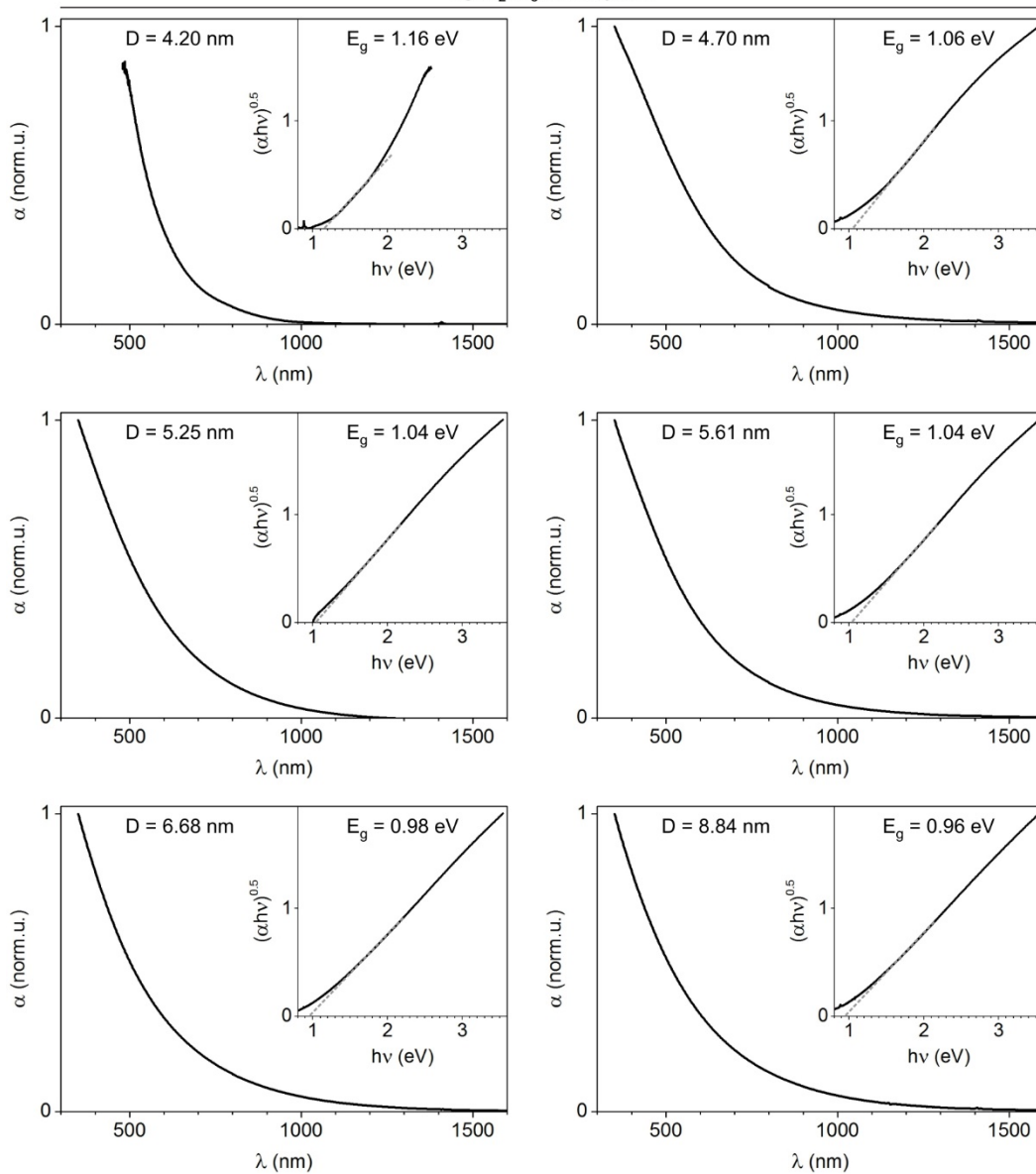


Figure S12. Absorption spectra and Tauc plots for AgSb₂Se₃ nanocrystals with different average sizes.

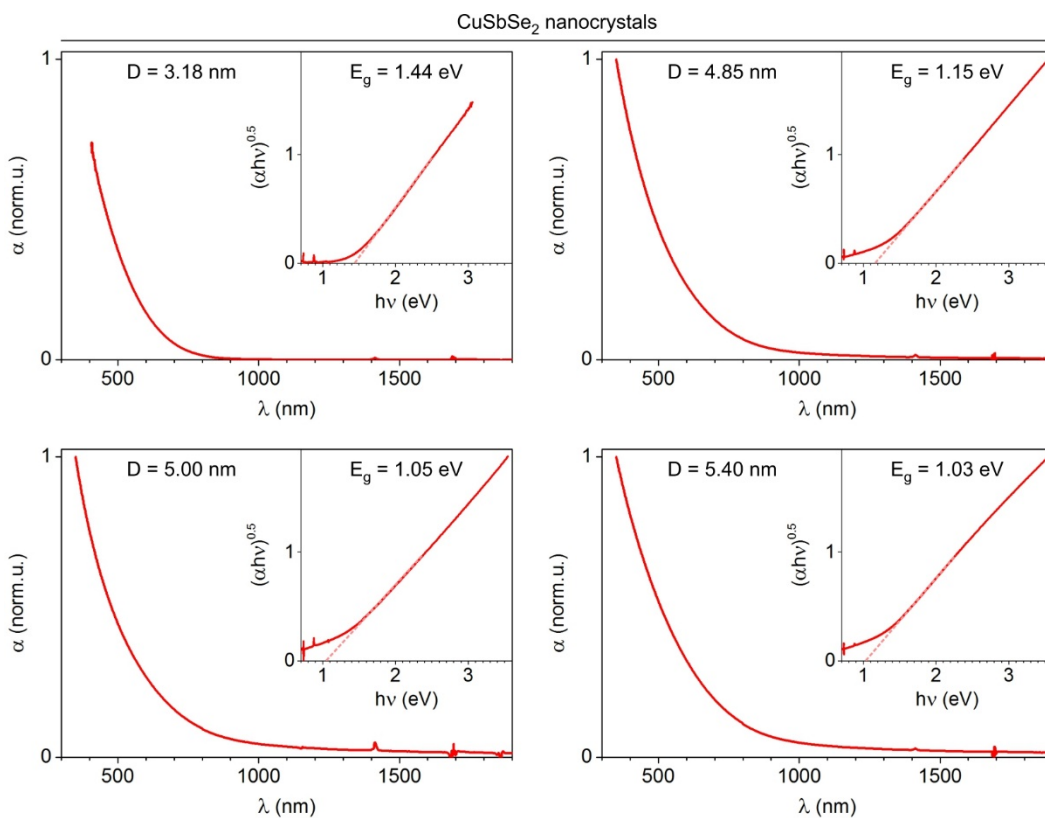


Figure S13. Absorption spectra and Tauc plots for CuSbSe₂ nanocrystals with different average sizes.

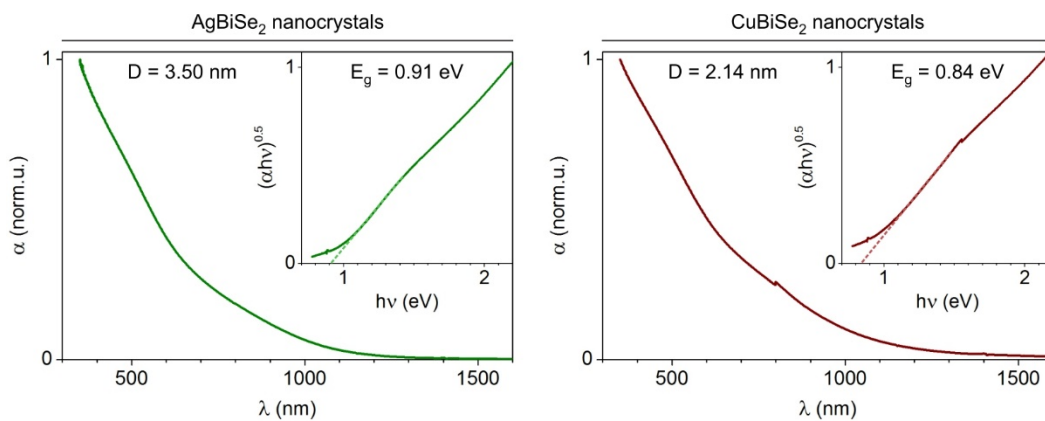


Figure S14. Absorption spectra and Tauc plots for AgBiSe₂ and for CuBiSe₂ nanocrystals.

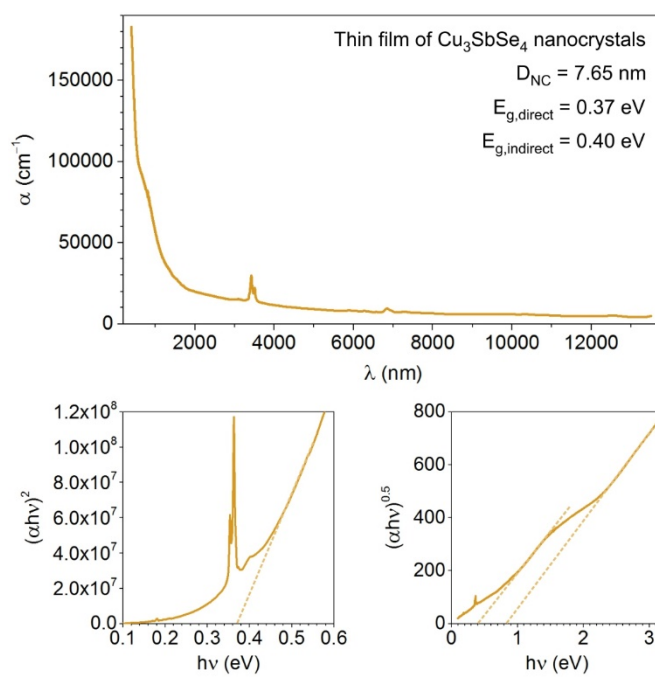


Figure S15. Absorption spectrum and Tauc plots for thin film of Cu_3SbSe_4 nanocrystals, cross-linked with 1,2-ethanedithiol.